International Journal of Hydrogen Energy 215 (2026) 153776

Contents lists available at ScienceDirect

International Journal of Hydrogen Energy

journal homepage: www.elsevier.com/locate/he

Insights on mechanical and morphological metal hydride powder characteristics during hydrogen interaction and stress mitigation strategies for hydrogen storage vessels

G. Stahlkopf [a,b], M. Passing [a,b], J.A. Puszkiel [a,b,*], J. Moosmann [c], F. Beckmann [c], J. Warfsmann [a,b], F. Karimi [a], V. Kulvait [c], T. Klassen [a,b], J. Jepsen [a,b]

[a] Helmholtz-Zentrum Hereon, Institute of Hydrogen Technology, Max-Planck-Straße 1, 21502, Geesthacht, Germany
[b] Helmut Schmidt Universität - University of the Federal Armed Forces Hamburg, Institute of Materials Science, Holstenhofweg 85, 22043, Hamburg, Germany
[c] Helmholtz-Zentrum Hereon, Institute of Materials Physics, Max-Planck-Straße 1, 21502, Geesthacht, Germany

ARTICLE INFO

Keywords:
Metal hydride
hydrogen storage
hydrogen
Mechanical stress upon phase transformation

ABSTRACT

Interstitial metal hydride alloys exhibit significant volume changes between the hydrogenated and dehydrogenated states during cycling, resulting in macroscopic stresses in powder beds that must be considered in tank design. Interactions are complex, and these stresses are primarily influenced by the local particle size distribution (PSD) and packing density. This study examines radial expansion forces in vertical storage containers using AB_2-type hydride alloys and synchrotron-radiation micro-computed tomography (SRμCT). Up to 50 cycles, progressive particle decrepitation occurs, with densification in the lower layers reaching a 91% packing density. This results in local pressures of up to 605 bar in the hydrogenated state. A new empirical equation links packing density to exponentially increasing stress. Experiments have shown that optimized PSDs can reduce stress by up to 45% and increase storage capacity by 87% within the same tank volume.

1. Introduction

On the pathway to a zero-emission infrastructure in the near future, renewable sources, such as solar, wind, and water power, have to be increasingly implemented. To overcome fluctuations and provide energy resilience and security, efficient and safe energy storage is essential for both the short and long term. Hydrogen is envisioned as the ideal energy carrier with high flexibility in energy distribution, storage, and use [1,2]. Depending on the degree of electrification, estimates for hydrogen demand across all sectors in the EU27 + UK by 2050 range from 161 TWh [3] to 2800 TWh [4]. Based on a lower heating value of 33.33 kWh/kg, this translates to hydrogen quantities ranging from 4.8 to 84 million metric tons. Hydride-forming materials have generated growing interest, as they can provide efficient, loss-free, and safe hydrogen storage at mild temperatures ranging from 0 to 80 °C and low pressures of up to 50 bar [5–7]. Moreover, metal hydrides (MH) offer a high volumetric storage density, such as Mg_2FeH_6 (150 kg H_2/m^3), considerably surpassing the corresponding values of pressurized gaseous hydrogen at 700 bar (40 kg H_2/m^3) and liquid hydrogen at −253 °C (71 kg H_2/m^3) [1,3,8]. This superior volumetric density makes MHs exceptionally promising for both stationary and mobile, compact hydrogen storage applications [9].

Although MH materials offer high volumetric hydrogen density, storage systems must be optimized for capacity, minimal weight and volume, operational reliability, and long lifespan. Volume expansion of up to 30 % [10] can generate critical stresses, potentially causing elastic and even plastic deformation, which must be avoided. Stress tends to accumulate at lower container sections during cycling due to powder bed decrepitation [11]. Coping with this “swelling/contraction' or “breathing' effect remains a key challenge in designing systems for maximum volumetric efficiency and is addressed in various studies.

To manage expansion during hydrogen cycling, metal hydride containers are typically filled to only 40–60 % of their volume, leaving void space to relieve internal stress [10,12,13], though this reduces volumetric efficiency. Structural strategies such as wall reinforcement, multi-layered container designs [14], and powder bed segmentation [14] help distribute stress more effectively. Material-based approaches include friction-reducing additives such as graphite, aluminium, and polymer coatings [15–17], which decrease wall stress but can reduce hydrogen capacity by up to 30 %. Pelletization with expanded natural

* Corresponding author. Helmholtz-Zentrum Hereon, Institute of Hydrogen Technology, Max-Planck-Straße 1, 21502, Geesthacht, Germany
E-mail addresses: julian.puszkiel@hereon.de, julianpuszkiel1979@gmail.com (J.A. Puszkiel).

https://doi.org/10.1016/j.ijhydene.2026.153776
Received 8 January 2026; Accepted 28 January 2026
Available online 6 February 2026

graphite (ENG), however, can enhance volumetric capacity by up to 150 % [17]. Glidants such as silicone oil, MoS_2, and carbon black improve powder flowability and reduce radial stress [18–22]. While effective, these strategies often compromise gravimetric and volumetric efficiency due to added inert mass or design complexity.

Radial stress and packing fraction are also influenced by particle alignment and settling. Okumura et al. [23,24] used computed tomography (CT) scans to reveal an inhomogeneous particle distribution after cycling, with the packing fraction correlating to the powder bed height within the container. Okumura [24], Escobar et al. [25] and Tran et al. [26] attribute this to settlement effects from pulverization, leading to densification in lower layers, increased packing fraction, agglomeration, and radial stress. Okumura et al. [13] recently confirmed ongoing densification at the bottom of $LaNi_5$-filled holders with repeated cycles. However, if the packing fraction remains below 61 %, with swelling-induced stress on the container remaining negligible.

Powder densification effects can be reduced by optimizing container design, such as lowering the cell's slenderness ratio S_r (height-to-diameter), as demonstrated by Tran et al. [26] and Gillia [10]. A high S_r stabilizes the powder bed via wall friction, reducing gravimetric forces on lower layers [27]. However, it can also hinder upward powder movement, limiting the bed's ability to “breathe' and increasing radial stress. In addition, the greater the difference between the radial and length dimensions, the less active material can be contained with respect to the container wall material, thereby decreasing the mass-related overall system storage capacity.

Lin et al. [28] also observed increased stress when using larger Mg_2Ni particles and high packing fractions. After 50 cycles, pulverization reduced the particle size to approximately 1 μm, causing agglomeration and a decrease in hydrogen capacity. Similarly, Haas and Schott [29] reported up to 50 % capacity loss in $Ti_{0.98}Zr_{0.02}V_{0.43}Fe_{0.09}Cr_{0.05}Mn_{1.5}$ under 100 MPa compressive stress. Borzenko et al. [30] linked this to metal lattice distortion.

However, even at low initial packing fractions, stress can increase rapidly and unpredictably [31], highlighting the complexity of swelling. This behavior results from multiple interacting factors, not just the packing fraction, S_r, or particle size, as outlined in Fig. 1.

The decrepitation of metal hydrides during hydrogenation cycles causes a continuous rearrangement of the powder bed, altering its mechanical properties [32]. This process continues until a final state is reached [25,33] if the material does not exceed the yield strength of the container during the cycling.

Despite decades of research, a comprehensive analysis of swelling-induced stress during hydrogenation-dehydrogenation cycles, along with viable solutions, remains limited at both micro- and macroscales. This study investigates how powder bed properties, including particle size distribution, packing fraction, alignment, and radial stress, evolve and interact upon cycling. This approach aims to reduce radial stress without the use of additives or altering the vessel's structure, thereby enabling more efficient volume utilization, higher storage capacities, and controlled elastic radial expansion. Unlike previous work focused on additives, little attention has been given to modifying the material or its morphology.

The following main strategies were pursued.

1. Investigating the powder bed inside the sample holder using synchrotron-radiation micro-computed tomography (SRμCT) images obtained from the *Deutsches Elektronen-Synchrotron* (DESY) and its relation to the measured expansion stress.
2. Investigating the powder after extracting it from the sample holder, separating it into the top, middle, and bottom powder layers using characterization techniques such as scanning electron microscope (SEM) and particle size distribution (PSD).
3. Engineering the metal hydride powder design to prevent stress accumulation behavior upon cycling.

2. Materials and methods

2.1. Material

All experiments were performed with the commercially available C-14 Laves AB_2 alloy *Hydralloy C5*® ($Mn_{51}Ti_{28}V_{14}Fe_3Zr_3$[1]) by GfE Metalle und Materialien GmbH. The achieved capacity in the lab was 1.6 to 1.7 wt% at a 40 bar H_2 pressure and 40 °C, following initial activation (initial hydrogen absorption cycles to improve its efficiency for hydrogen uptake). The volume expansion of the crystal lattice in the absorbed state is 21.3 % [34]. The initial powder forms used for the experiments are listed in Table 1.

2.2. Sample preparation

If not labeled differently, the powder samples were loosely filled into the sample holder (SH) (Fig. 2c–f). Compacted samples ("comp') were made by gradually filling the SH with metal hydride powder and manually compressing it using a hammer and screw, which also released trapped gas from the pores of the powder bed. Only the borehole could be compacted, not the cone (Fig. 2d and e). "MaxCompFill' samples contain the maximum compacted powder in the borehole (Fig. 2d). The Packing fraction (Φ") was determined by measuring powder bed height after filling with a caliper. The packing fractions were calculated according to equations (1)–(3) introduced by Gillia [10]:

Solid volume related to powder bed volume:

$$\Phi = \frac{V_s}{V_{hb}} \quad (1)$$

Solid volume related to cell volume:

$$\Phi' = \frac{V_s}{V_{cell}} \quad (2)$$

Powder bed volume related to cell volume:

$$\Phi'' = \frac{V_{hb}}{V_{cell}} \quad (3)$$

with the solid volume V_s of the active material, the powder bed volume, including its porosity V_{hb} and the empty cell volume of the storage container V_{cell}. In an additional experiment, the cone of the sample holder was filled, labeled in the following with “*MaxFill*' (Fig. 2e), achieving a maximum filling of $\Phi'' = 1$. The conical section was loosely filled and leveled to just below the sealing disc at the system interface.

The used *Hydralloy C5*® was crushed employing a jaw crusher *Retsch BB50* with a jaw width of 2 mm. From the crushed material, different PSDs were achieved by dry sieving using a sieve tower, *Analysette 3 Pro* by *Fritsch*, with mesh sizes of 20, 32, 40, 63, 80, 100, 125 μm, 1, and 2 mm. The sieving of the already activated material was done inside a MBraun 200B Eco glovebox (working atmosphere: $O_2 < 2$ ppm, $H_2O <$ 0.5 ppm).

The PSDs were measured using the *SYNC* from *Microtrac*, based on laser diffraction and employing the wet dispersion method (1:200 tetrasodium pyrophosphate, Na4P2O7, in a demineralized water solution).

To separate agglomerates, the powder samples were exposed to an integrated ultrasonic (US) treatment for 180 s before the PSD measurement. As determined by laser diffraction, the particle diameter corresponds to the diameter of an ideal sphere that scatters light in the same way as the measured particle.

[1] chemical composition in wt%.

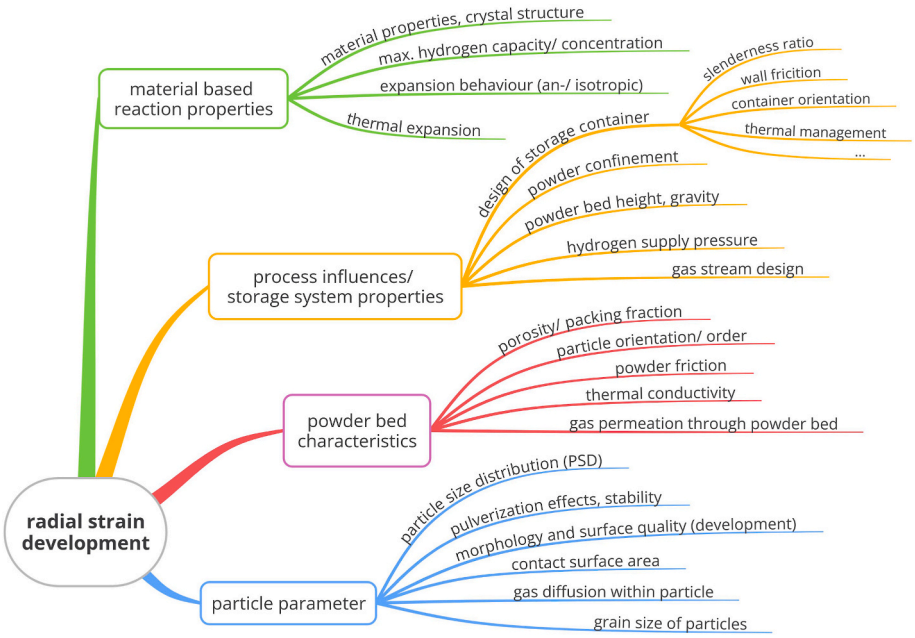

Fig. 1. Overview of influencing factors for the stress development during hydrogen absorption of metal hydrides.

Table 1
Sample overview and designation of Hydralloy C5® for the performed experiments.

Designation	Sample origin	Sample pre-treatment, sample specifications, (Activation)/titration parameters	Characterization techniques	Sample holders
Crush-S1-2	crushed *Hydralloy C5*® (Crush) - jaw crusher, jaw width 2 mm	- Particle size sieved 1-2 mm - Titration cycles: ▪ Abs.: 40 bar, 40 °C, 1 h ▪ Des.: 1 bar, 40 °C, 0.5 h	- Titration + radial stress meas. - Measurement in the oxidized state: ▪ PSD-Measurement (180 s US) ▪ SEM	- Medium sample holder (m) - Small sample holder (s)
Crush-A5T-S_x-y	crushed *Hydralloy C5*® (Crush) - jaw crusher, jaw width 2 mm	- activated (A) – 5 titration cycles (5T) in a big container - separated PSD by sieve tower ▪ Mesh-sizes: x-y ∈ {x, y [µm]|0-20, 20-32, 32-40, 40-63, 63-80, 80-100, 100-180} (S) - Titration cycles: ▪ Abs.: 40 bar, 40 °C, 1 h ▪ Des.: 1 bar, 40 °C, 0.5 h	- Titration + radial stress meas. - Measurement in the oxidized state: ▪ PSD-Measurement (180 s US)	- Small sample holder (s)
Crush-A5T-S-O2_x-y	crushed *Hydralloy C5*® (Crush) - jaw crusher, jaw width 2 mm	- activated (A) – 5 titration cycles (5T) in a big container - separated PSD by sieve tower ▪ Mesh-sizes: x-y ∈ {x, y [µm]|0-20, 20-32, 32-40, 40-63, 63-80, 80-100, 100-180} (S) - oxidized (O2)	- Measurement in the oxidized state: ▪ PSD-Measurement (180 s US)	
Mix Crush-A5T-S_80-100 + C1-2		- Mixture: 70 % Crush-A5T-S_80-100 +30 % Crush1-2 in middle layer	- Measurement in the oxidized state: ▪ PSD-Measurement (180 s US)	- Small sample holder (s)
Designation additions: - _comp.: compacted manually - _MaxCompFill: max. Possible, compacted filling height in the SH borehole - _MaxFill: additional to _MaxCompFill loose filling of cone		- _s: small sample holder used - _m: medium sample holder used - _#n: number n of titration cycles	- _bot: Strain gauge measurement at the bottom part of the sample holder - _mid: Strain gauge measurement at the middle part of the sample holder - _top: Strain gauge measurement at the top part of the sample holder	

Sample holder Designation	**Inner diameter x wall thickness x height**	**Slenderness ratio S_r (h/d)**	**Strain gauge position**	**Volume V_{cell}**	**Material**
1. Small (s)	4 x 1.25 × 35 mm	8.75	bottom, middle, top layer	0.403 cm^3	1.4404/AISI 316L
2. Medium (m)	12 x 1.5 × 35 mm	3	bottom layer	4.175 cm^3	

2.3. Sample holder and stress measurements

Two different sample holder (SH) dimensions were used (Fig. 2g and h, geometry in Table 1). The small SH (sSH, Ø6.5 mm) matched the beamline's limits in terms of dimensions, resolution, and safety. The strain gauges DMS 1.5/350 LY45 (for sSH) and DMS 6/350 LM15 (for medium SH (mSH)), manufactured by HBK, with tolerances of ±0.75 % [35] and ±0.7 % [36], respectively, were glued to the outer wall in a peripheral direction. Elongation is expressed in micrometers per millimeter (µm/m). The measured strain is converted to an equivalent inner pressure x_{bar} in bar, representing the radial stress of the metal hydride powder inside [37]. Both expressions will be used synonymously in the

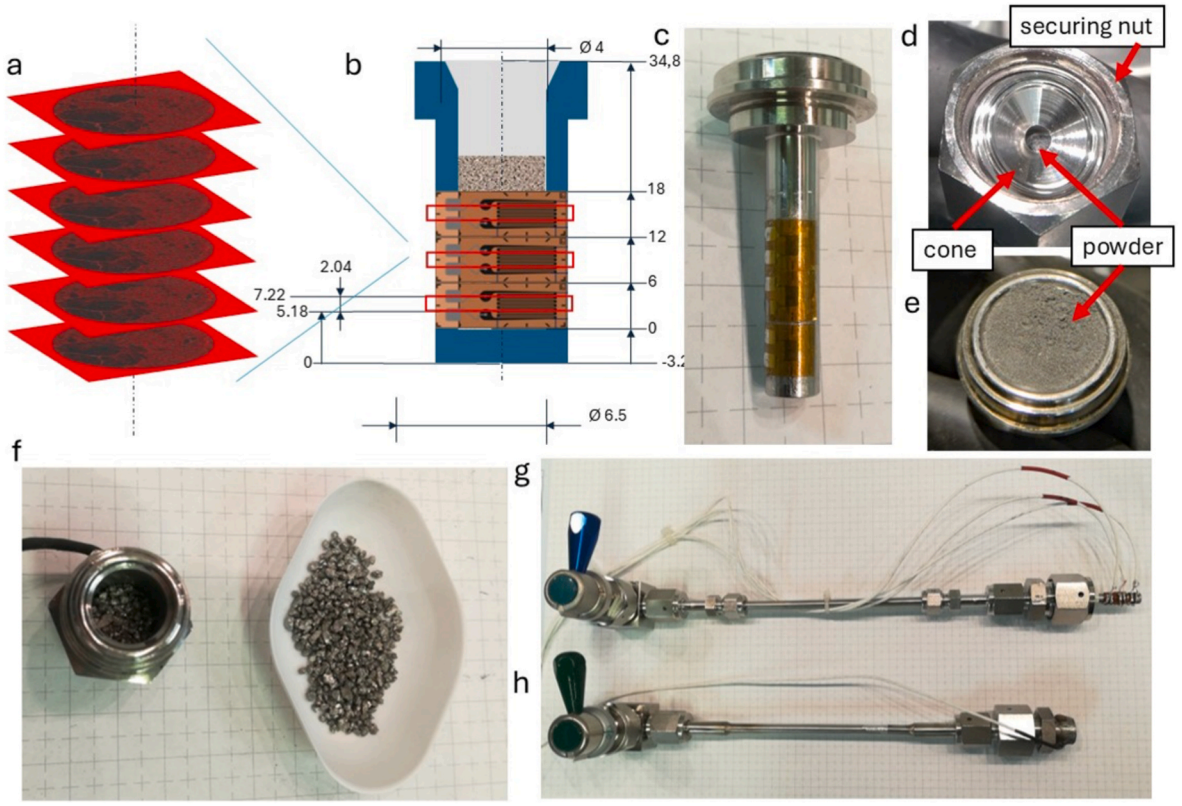

Fig. 2. a) SRμCT scan results after the data reconstruction and processing. b) sketch of the sSH and positions of the strain gauges, in red, marked the scan field of the CT. c) Picture of the used sSH with mounted strain gauges. d) sSH in the "maxCompFill' state. E) sSH in "MaxFill' state f) Initial state of a loosely filled medium-size sample holder. g) Assembled small sample holder and h) medium sample holder used for the titration devices. (For interpretation of the references to colour in this figure legend, the reader is referred to the Web version of this article.)

following. The experiments were stopped before reaching the yield strength of the SH walls.

The strain gauges for the sSH were placed at three different heights. The lowest strain gauge position was 3.2 mm above the bottom of the sSH to diminish its influence on the geometrical stiffness of the radial expansion (see Fig. 2b). A finite element simulation by *COMSOL Multiphysics 6.2* was done to determine this minimum height of the strain gauge (see supportive information (SI) Error: Reference source not found). The middle and top strain gauges, each with a height of 6 mm, were placed directly on top of each other. The same calculation was carried out for the mSH, where the single strain gauge was placed at 5 mm above its bottom (Fig. 2h).

2.4. Titration measurements

The absorption and desorption processes were carried out in an in-house-designed Sievert apparatus. For the absorption measurement, the sample holder was heated to 40 °C. The absorption and desorption pressures are 40 and 1 bar of hydrogen (purity 5.0), respectively. The titration parameters are listed in Table 1. The SH is mounted vertically. Due to the device's setup, the pressures between the sample and the reference volumes equalize within the first 100 ms at the beginning of each absorption and desorption process. After this period, these volumes are separated to initiate the measurement, resulting in the loss of the first measuring points of the reaction. This leads to an increased systematic deviation due to the fast kinetics of the used metal hydride alloy and a reduced hydrogen capacity of approximately. 1.2 to 1.4 wt% is typically recorded. The measurement error of the device is ±0.007 wt% and ±0.06 wt% for the mSH and sSH, respectively, according to the law of error propagation.

The full expected capacity of the material could be measured during the first activation cycle, reaching an average maximal hydrogen capacity of 1.66 wt%. Additionally, after the titration experiments, the maximum capacity was measured exemplarily for one sample (after 15 cycles). The sample was frozen in its absorbed state using liquid nitrogen. Subsequently, the desorption was initiated from the frozen state by slowly heating it to room temperature. Consequently, the measurement inaccuracies of the setup could be avoided, and a maximum capacity of 1.72 wt% was measured.

2.5. SRμCT preparation, measurements, and analysis

Six sSHs prepared for the Synchrotron-radiation-micro-computed-tomography (SRμCT) were loosely filled (Fig. 2c) with the same powder mass of 0.825 ± 0.001 g, which resulted in the packing fractions of $\Phi = 45\,\% \pm 0.5$, $\Phi' = 24\,\% \pm 0{,}1$, and $\Phi'' = 54\,\% \pm 1.8$. Due to the loose filling, the particle arrangement is random, and the initial height of the powder bed varies, as mentioned. The sSH were cycled 0 (not activated), 5, 10, 16, 20, and 26 times, respectively. Each last cycle was stopped in the absorbed state under a hydrogen pressure of 40 bar. The cycles were performed 3 days before the SRμCT measurements to minimize relaxation effects. SRμCT was performed at the high-energy materials science (HEMS) beamline P07, operated by *Helmholtz-Zentrum Hereon*, at the storage ring PETRA III at DESY, Hamburg, Germany [38].

The experiment utilized conventional attenuation contrast imaging with a photon energy of 103 keV (wavelength of 0.12 Å). For each sample, 5001 projections were taken over 180°, with an exposure time of 200 ms per projection. Imaging was performed using an indirect detector system converting X-rays to optical light using a $CdWO_4$ scintillator. The optical light was then magnified by a microscope optic and

detected with a camera with a CMOSIS chip, developed in-house by KIT and Hereon [39]. The camera offers a resolution of 5120 × 3840 pixels with a pixel size of 6.5 × 6.5 µm, positioned 300 mm behind the sample. To ensure accuracy, dark and flat-field images were captured separately for each scan. A magnification of 5 was applied, resulting in a pixel resolution of 2.55 µm after 2x binning and a reduced field of view (FOV) measuring 6.52 mm × 2.04 mm (Fig. 2b – red windows). The resolution of the scans could resolve particles down to approximately 7 µm in size, depending on the local compaction level.

CT scans were performed on the as-prepared absorbed state for each strain gauge (bottom, middle, and top layer) and SH. The scans were recorded at the middle of each strain gauge to directly relate the measured expansion stress at each layer to the powder bed properties. Two more scanning series were performed after first reducing the hydrogen pressure to the half-desorbed state at 9 bar at room temperature. Approximately 50 % of the maximum capacity (averaged 0.63 wt %, considering the reduced measured capacity mentioned earlier, see SI Error: Reference source not found) was reached. Lastly, the fully desorbed samples were measured after evacuating the hydrogen pressure.

The data reconstruction was performed at the beamline (see Ref. [40] for details) and 800 cross-sections with a 2.55 µm distance between each other were reconstructed (Fig. 2a).

To calculate the packing fraction for each cross-section, a *MATLAB* algorithm was developed (see SI Error: Reference source not found), which automatically detects the inner wall of the sample holder to separate the powder bed from the sample holder's wall for 50 cross-sections in the middle of the strain gauge. Afterwards, it selects the particle pixels from the void space within the powder bed by using an empirically determined, constant threshold (SI Error: Reference source not found). By this pixel evaluation, the local packing fraction Φ_{local} at each cross-section is calculated (relation particles to void space) and averaged. It is related to the measured expansion stress at 40 bar in the absorbed state, as determined from prior cycling measurements.

2.6. SEM measurements

Scanning electron microscopy (SEM), using a FEI Quanta 650, was employed to examine the particles and their morphological changes. For this, the powder was oxidized for 1 week by slowly letting ambient air diffuse into the powder bed. The samples were placed on conventional aluminum mounts via graphite planchets and sputtered with gold. A voltage of 20 kV and a magnification from 50 to 20,000 were used.

3. Results

3.1. SRµCT measurements

Fig. 3 shows the results of the SRµCT images in the form of horizontal (a–d) and vertical (f–h) cross-sections. Based on the SRµCT data analysis, the local packing fraction was calculated for both the absorbed and desorbed states, and is presented in Fig. 3e for the complete powder bed height.

- The powder bed exhibited increased porosity during the transition from the absorbed to the desorbed state (Fig. 3e) and a significantly reduced powder bed height of approximately 38 %, which can be attributed to a 21.34 % shrinkage of the particles [8].
- During desorption and particle shrinkage, the formation of relatively large gaps occurred (of approx. 320 µm width in #26, Fig. 3h-(1)) between agglomerated areas, particles, or between still-in-initial-shape larger particles[2] (Fig. 3a (2), h(3)). These gaps allow fine particles to fall in and settle into deeper layers, resulting in a more compacted powder bed with higher radial stress in this area, as can also be seen in Fig. 3e. This is in accordance with the results reported by Lin et al. [41].
- The initially 1-2 mm large particles broke and crumbled significantly within the first 10 cycles (Fig. 3a). Pulverization occurs predominantly in the top section, while larger particles are still visible in the middle and bottom sections (Fig. 3b–d). Fine particles (<5 µm), detected throughout the powder bed after five cycles by PSD analysis (see SI, Fig. S6), promote the agglomeration and cohesion of the particles.
- Larger particles (1–2 mm) remained mainly in the lower and middle bed sections even after 26 cycles (Fig. 3b–d). In desorbed and half-desorbed states, they show cracks (5–20 µm, Fig. 3c-(4)) but retained their shape. Some cracks trapped smaller particles, potentially hindering closure during absorption and promoting further breakage. In other regions, advanced fragmentation indicated progressive crumbling into finer powder (Fig. 3c-(5)).
- The pulverization and detachment of fine particles usually proceeded from the outside to the inside of the particle (Fig. 3a-(9)) or by separation of a larger fraction of the particle (Fig. 3d-(9)). These larger particles in the bottom or middle layer were surrounded by fine powder, preventing them from falling apart even in a fractured state (Fig. 3b–d, bottom). This resulted in a locally high density and packing fraction, leading to high radial stress (Fig. 3). The local packing fraction of these supported particles (Fig. 3d (7)) and the fine powder clusters (Fig. 3d (8)) was approx. 91 % and 64 % (top layer) to 70 % (bottom layer), respectively.
- After extracting the powder and analyzing it in SEM, the larger particles visible in the SRµCT cross-sections were found to be a mix of supported particles and agglomerates (Fig. 4b and c).

Consequently, the packing fraction increased from top to bottom (Fig. 3e), and high confinement appeared to prevent pulverization.

While the general conclusions were reproducible in other specimen holders, the concrete arrangement, size, and agglomeration density of particles varied somewhat from sample holder to sample holder, supporting the assumption of non-reproducible powder bed development and randomness, which can give rise to unpredictable stress increases within a certain number of cycles. The #20 cycled sample holder in this series showed the highest compaction.

During desorption, the powder bed shrank into a single, large cylindrical agglomerate, creating an annular gap in the inner wall of the sample holder (Fig. 3a - (6)). Cracks inside bigger particles or agglomerates either expanded or sometimes also shrank again from the half-desorbed state to the fully desorbed state. The compaction and stability of powder bed agglomerates increased in the lower sections within the powder bed. At the bottom, the powder bed shrank uniformly and maintained a cylindrical shape, creating a gap between the bed and the walls, with a maximum gap width of 50 - 68 µm in the desorbed state (Fig. 3a, vacuum). The top layer exhibited a more pronounced instability, resulting in higher fragmentation compared to the middle section.

For higher-resolution analysis of particle morphology, agglomerates, and stabilized structures, SEM images were taken at various cycling stages (Fig. 4a). The fracturing and decrepitation of the particles are obvious and increase with increasing cycling number. The particle size analysis confirmed this (see SI Error: Reference source not found). The cracks showed gap sizes in the single-digit micrometer scale (<3.5 µm, SEM micrographs, SI Error: Reference source not found). At higher cycling numbers, the fine particles (<5 µm) started to agglomerate, and smaller particles were attached to bigger ones (>50 µm scale) or formed agglomerates of smaller particles (Fig. 4b). These results are in good agreement with the observations reported by Blinov et al. [42]. The particles showed a rough, cracked surface and a sharp-edged shape. Despite the visible cracks, the larger fractured particles remained partially interlocked. Despite the externally acting compression forces,

[2] Particles, that didn't change their size during cycling. They are fractured inside but stay stable interlocked in themselves, but didn't form a new agglomerate.

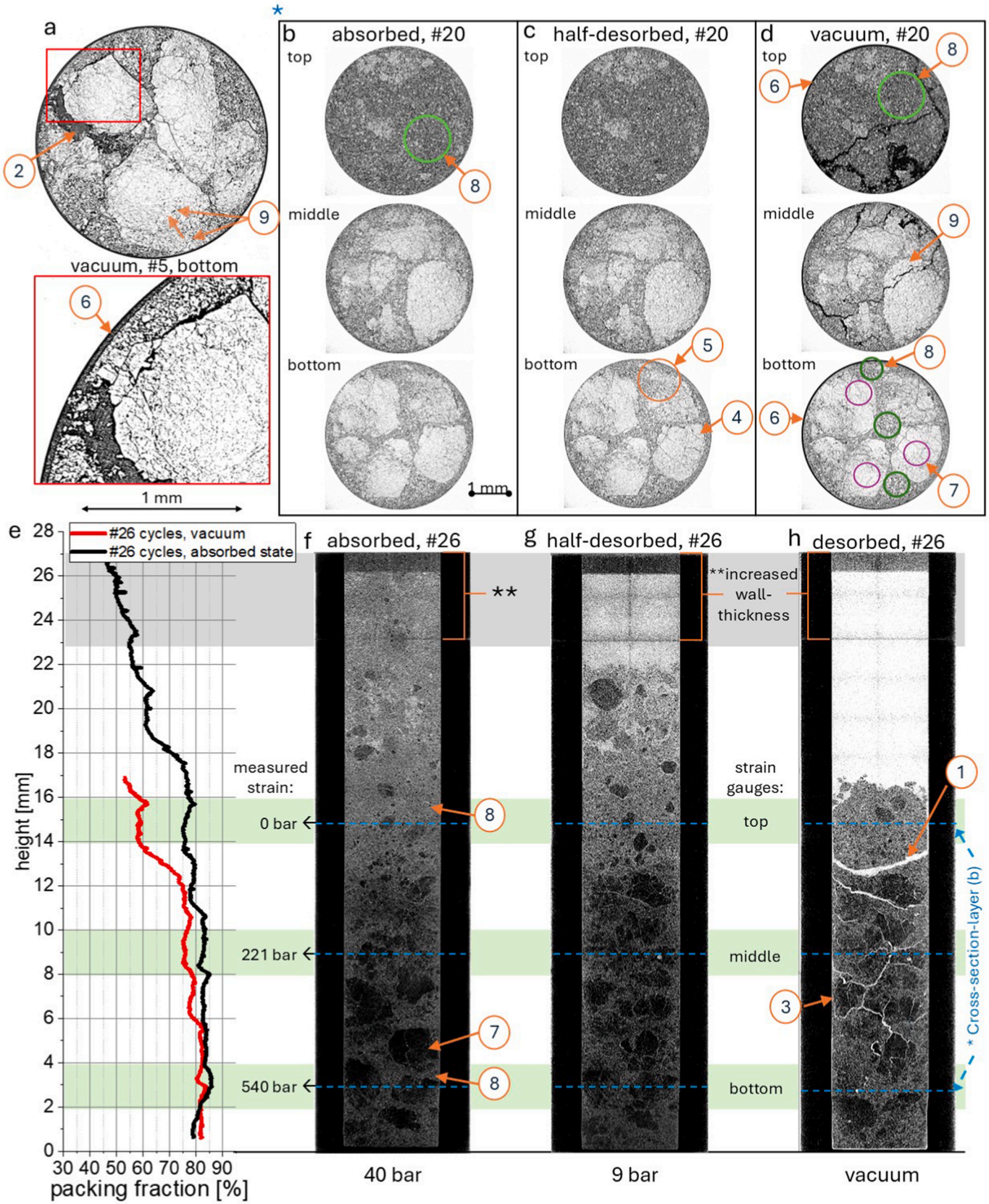

Fig. 3. a) After 5 cycles in vacuum, the cross-section of the top layer with significant gaps within the powder bed and between the agglomerated powder bed and the wall b-c) Cross-section from the bottom, middle and top layer after 20 cycles at different saturation states e) Development of the packing fraction over the height of the powder bed shown in f-h, which display the 3D reconstructions of the powder bed after 26 cycles.

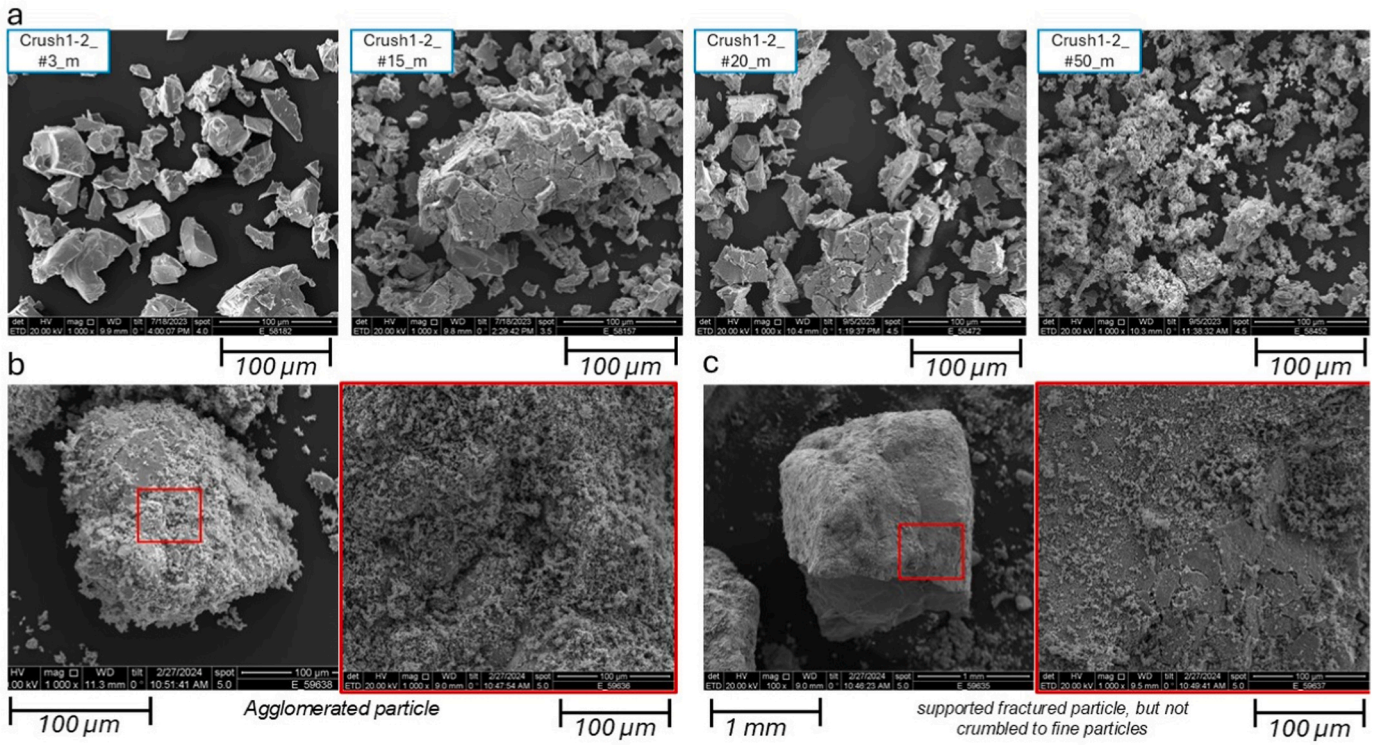

Fig. 4. a) Development of cycled MH particles after different cycle numbers (#x) extracted from the middle layer. b) Agglomerated particle and c) supported, fractured, but still-in-shape-particle after 20 cycles from the bottom layer.

agglomerates form due to adhesion and van der Waals forces [27] (Fig. 4f).

3.2. Particle size distribution

The volume-weighted particle size distribution measurements of *Crush-A5T-S_20-32_s_MaxCompFill* showed only a slight change as compared to the initial bimodal PSD after the 5 activation cycles (Fig. 5a), after 34 cycles (Fig. 5b). The bottom and middle layers showed a slight increase in the number of particles between 1 and 5 µm particle size without decreasing the minimum particle size. The top layer transitioned from a bimodal distribution to a monomodal distribution, resulting in an increase in the amount of very fine particles, with a peak at 3 µm. The bimodal PSD of *Crush-A5T-S_80-100_s_MaxCompFill* also showed a decrease in the larger particles towards the final particle size, with a peak at 5 µm.

Analysis of the PSD after different cycle numbers revealed a trend toward a minimum particle size. A lower mean particle size limit was observed, which is referred to as the final particle size. The PSD of the mSH's powder *Crush-S1-2_m_#50* (Fig. 6) reached a minimum, final particle size after 50 cycles in the d_{50} range of 5.4 µm, 7.1 µm, and 4.2 µm for the bottom, middle, and top layer, respectively (see SI Error:

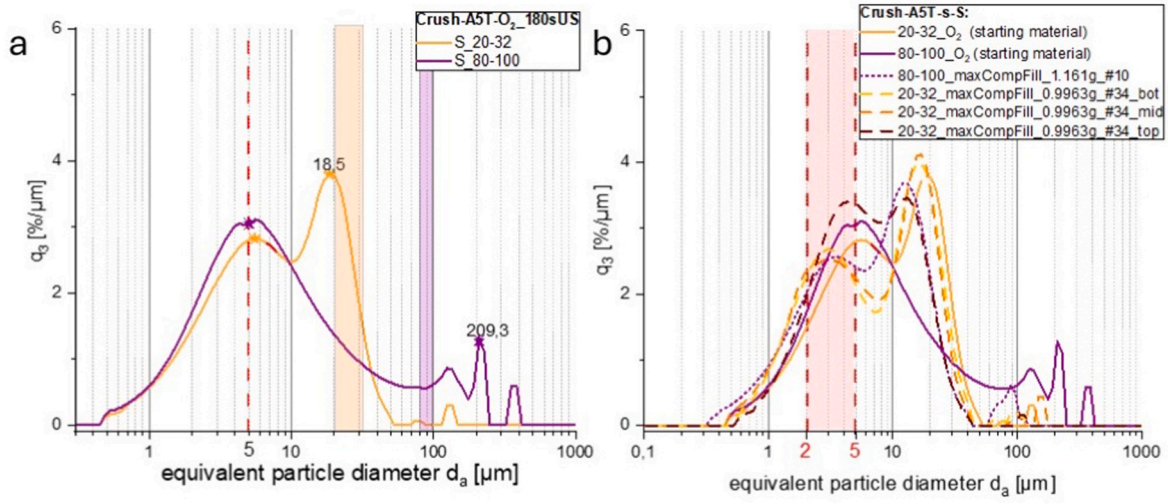

Fig. 5. a) PSD of activated (5 cycles), oxidized, sieved Hydralloy C5® as starting materials for the titration experiment in the displayed sieving ranges (highlighted columns). c) Comparison of the selected PSD before and after the titration experiments, with the final particle size range marked in red. (For interpretation of the references to colour in this figure legend, the reader is referred to the Web version of this article.)

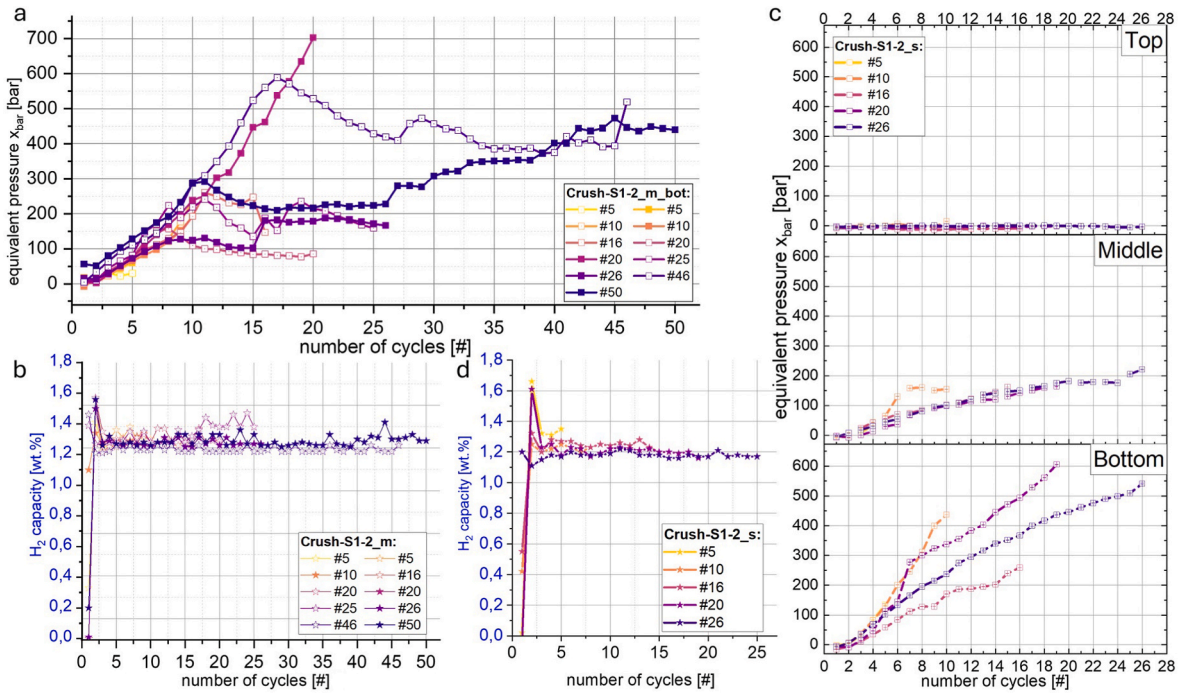

Fig. 6. a) Max. measured radial stress (converted to the equivalent inner pressure x_{bar}) and b) hydrogen uptake values for absorption cycles with equal 1-2 mm particles of 7.1 g in a medium sample holder and c) radial stress values of 0.825 g in a small sample holder and d) their hydrogen uptake.

Reference source not found). The bottom layer exhibited a broader PSD with an increasing number of cycles. The coarser particles existed longer than the middle and top regions, maintaining the broader PSD.

For the sSH after 26 cycles, more small particles in the 1-10 µm range were measured compared to the PSDs of the less cycled samples.

3.3. Stress development and hydrogen absorption

In this section, the influence of containment dimensions on stress development is investigated.

3.3.1. Medium sample holder (mSH)

The stress measurements of mSH (Fig. 2f and h) in dependency of hydrogenation-dehydrogenation cycles under equal initial conditions revealed a random pattern of stress development at the bottom layer (Fig. 6a). This confirms the conclusion made by several other researcher groups, summarized by Gillia [10], who also recorded similar stress developments. The achieved hydrogen capacity per cycle within the experiment series showed a constant average value of 1.28 ± 0.05 wt%, measured at 40 bar (see 2.4, Fig. 6b).

Initially, the stress increased similarly across the first 8 cycles for each experiment (see Fig. 6). However, the following cycles exhibited divergent stress developments. For example, sample *Crush-S1-2_m_bot_#20* exhibited a continuous increase in stress, reaching the safety limit of the sample holder's material after 19 cycles. It was stopped after 20 cycles to prevent plastic deformation. Conversely, sample *Crush-S1-2_m_bot_#46* showed a similar stress increase during the first 17 cycles. However, after 17 cycles, the expansion stress decreased temporarily before increasing again at cycle 27, displaying an up-and-down radial stress pattern with lower maxima than before.

This behavior, characterized by reaching a certain maximum stress value followed by a decrease and a fluctuating plateau, was also observed in other samples. However, this pattern was not reproducible and unpredictable, as it was unclear which sample would reach the safety limits after a specific number of cycles. Even though only one sample reached the safety limits of the container material, it was not predictable which of these samples would exhibit this behavior, as they had the same initial conditions.

3.3.2. Small sample holder (sSH)

Measurements analogous to mSH were performed using a sSH (Fig. 2c and g), which included two additional strain gauges in the middle and top layers. These sSH were scanned in SRµCT and are shown in 3.1. The titration cycles revealed a consistent hydrogen capacity independent of the developed expansion stress, averaging 1.21 ± 0.04 wt % (Fig. 6d). These values remained constant across all measurements with the sSH and were independent of the measured stress. The capacity was reduced by 0.07 wt% compared to the mSH. This could be related to an increased measurement error of ±0.06 wt% resulting from the smaller hydride mass. The capacity at 9 bar, which was used for an intermediate desorption step during the SRµCT scans (Fig. 3c–g), reached an average of 0.67 wt%, equivalent to a hydride fraction of 55 %.

The radial stress increased with each cycle, from top to bottom (see Fig. 6c), with the top layer exhibiting no radial stress. The maximum equivalent pressure is 605 ± 4.5 bar for the sample *Crush-S1-2_s_bot_#20* in the last cycle and in the hydride state. The bottom layer exhibited the steepest increase in stress. Like the stress measurements of the mSH *Crush-S1-2_m*, the stress curves showed deviations and were not reproducible or predictable. One measurement had to be stopped to prevent damage to the sample holder due to excessive radial stress development after 20 cycles (Fig. 6c, #20). Plastic deformation was excluded, as strain values returned to 0 % after each titration.

3.4. Stress development upon cycling with selected initial particle sizes

To investigate whether it was possible to minimize changes within the powder bed due to pulverization and densification effects, by using a low initial PSD, powder batches with a sieving range from 20 to 32 µm

and 80 – 100 μm (see Fig. 5a) were compared. Before sieving the powder, the material was activated and cycled 5 times. The selected PSDs were close to the final particle size of 2 to 5 μm, which was expected to result in more consistent behavior due to reduced pulverization during further cycling. The (dry) sieved batches include a larger amount of very fine particles (<10 μm), which could not be separated. The batch sieved between 20 μm and 32 μm shows a peak at 18.5 μm, whereas the 80–100 μm batch shows a broader PSD with a maximum particle size of 400 μm.

The powder bed packing fraction Φ was increased from 43 % for *Crush-A5T-S_20-32_s_maxCompFill* to a maximum of 60 % for *Mix Crush-A5T-S_80-100 + C1-2_s_comp*. This was done by using the particle size batch 80 – 100 μm (broader PSD) and adding 1-2 mm particles to the sieved powder (see Fig. 7 b).

By manual compaction during filling of the SH, the sample mass can be increased, and the packing fraction Φ′ increases from 25 % to a maximum of 46 % for *Crush-A5T-S_20-32*. A powder filling level of Φ" = 100 % was achieved with Φ' = 46 % (porosity of 54 %). The other samples reached packing fractions between Φ" = 40 % and 67 %.

Even though *Crush1-2_S20-32_A5T_MaxFill* (Fig. 2e) contained by far the biggest powder amount, the stress values compared to *Crush-S1-2* powders were extremely low after 20 cycles, with x_{bar} values < 52 bar for the bottom layer (see Fig. 7a). In the middle, the stress values were higher than with *Crush-S1-2* after 20 cycles, with 195 bar compared to 165 bar. At the top layer, the stress values of 330 bar were in the upper third compared to the other selected PSD samples. The stress values for *Crush-S1-2* samples were zero at the top layer due to a loose packing fraction (see 3.1). For the rest, the measured equivalent pressures were already partially significant in the first cycle, with values ranging from 50 to 1115 bar, 90 to 1390 bar, and 60 to 515 bar for the bottom, middle, and top layers, respectively.

The middle and top layers showed higher stress than the Crush-S1-2 powder after 25 cycles. *Crush-A5T-S_80-100_s_comp_MaxFil* and *Crush-A5T-S_80-100+C1-2_s_comp* showed high stress, containing bigger initial particles or a higher powder mass. They included a higher powder bed packing fraction of 54 % and 60 % and an initially lower porosity, respectively. The 1-2 mm particles in the latter sample were positioned in the middle layer of the sample holder, correlating with the highest radial stress measured in this layer, which imitates the phenomena observed in the 1-2 mm supported particles (Fig. 3d - (7)).

Interestingly, the radial stresses of 20-32 μm and 80-100 μm powder batches in Fig. 7a showed significant differences as compared to the measurements using *Crush-S1-2* powder (Figs. 7a and 6): After approximately 10 cycles, the expansion forces stayed constant and didn't increase significantly anymore, reaching a stable state after a small number of cycles. Initially, a particle of 1-2 mm in size (Crush-S1-2) exhibited a continuous increase in radial stress with increasing cycle

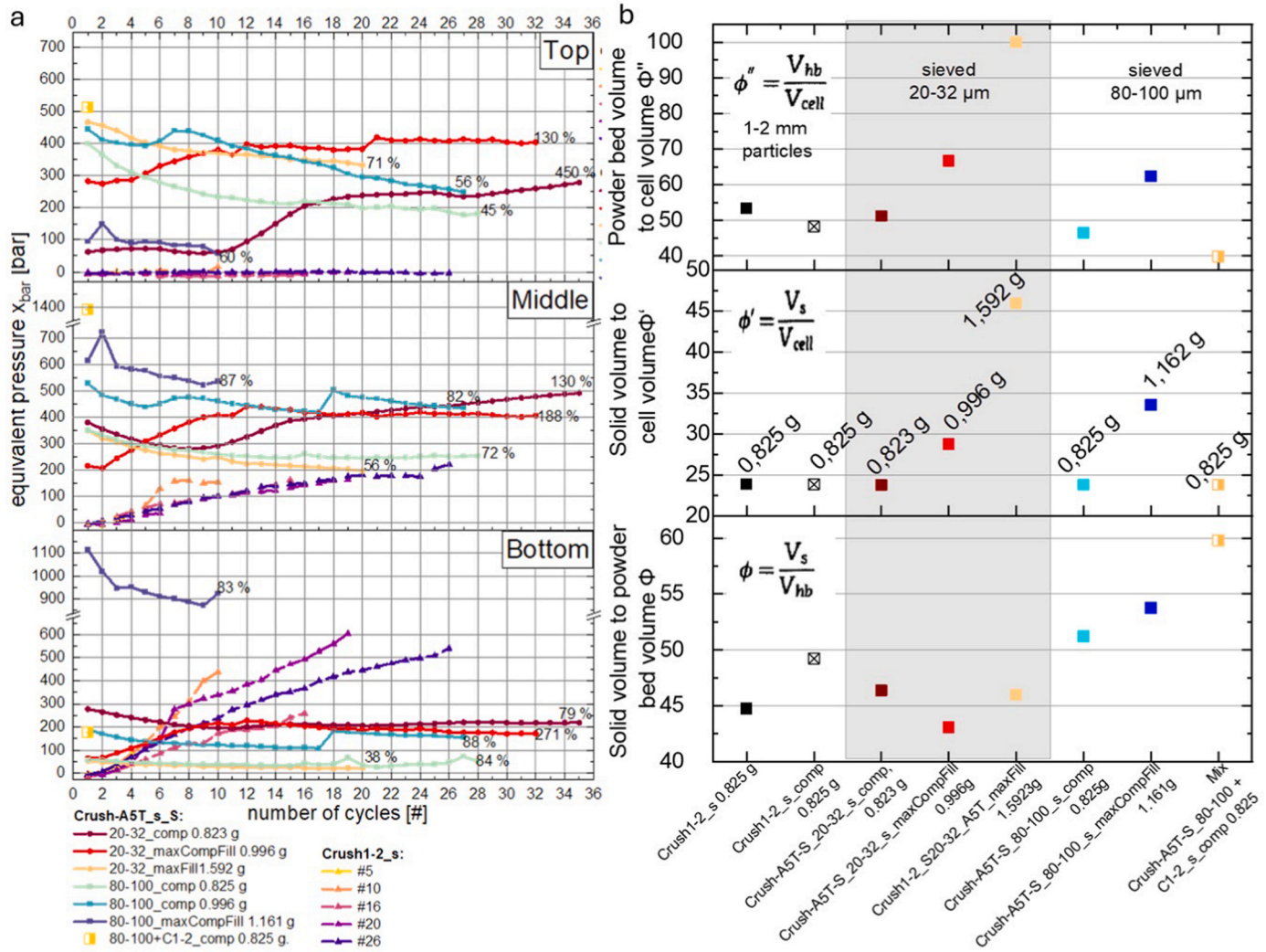

Fig. 7. a) Measured maximal equivalent pressures for each cycle of the sSH in three different heights (dotted lines represent the measurements of the sSH scanned with CT, same results as shown in Fig. 6c). The percent values indicate the increase or decrease in radial stress relative to the first cycle. b) Overview of the different packing fractions for the different experiments.

numbers, with maximum values in the bottom layer (Fig. 7, dotted lines). The PSD influenced stress development during the hydrogenation cycles. Sieved particles with a mesh size of 20-32 µm showed a slight increase in radial expansion values, while experiments with 80-100 µm particles consistently exhibited a downward trend. All developments here are relatively minor compared to the initial measurements with particles of 1-2 mm.

After cycling, the global packing fraction changed, and a loosening of the upper accessible powder layers was visible, indicating a slight increase in the powder bed heights. These loose upper layers prevented accurate measurement of the global packing fraction afterwards.

For the sample mass of 0.996 g for 20-32 µm and 0.996 g for 80-100 µm, the radial stress after 27 cycles shows similar values for the middle and bottom layers. The top layer exhibits higher values for the finer powder, achieving constant stress after 21 cycles, while the 80-100 µm batch shows a steady downward trend.

4. Discussion

4.1. Influence of the packing fraction

The evaluation of the scanned sample holders (S_r of 8.75) at various saturation hydrogenation states, hydrogenation-dehydrogenation cycles, and measured stress values revealed a strong influence of the local packing fraction, Φ_{local} (Fig. 3), on stress development (Fig. 6). Φ_{local} describes the calculated local packing fraction within a horizontal cross-section in the absorbed state of the sample holder, based on the SRµCT data (see calculation in SI Error: Reference source not found). X_{bar} increases exponentially after reaching a certain threshold of $\Phi_{local} = 70$ %, shown in Fig. 8.

The relation between the equivalent inner pressure x_{bar} (see 2.3) and the local packing fraction Φ_{local} based on the SRµCT data in a vertical sample holder (see 2.5) is described by the empirically developed Eqs. (4) and (5).

$$\Phi_{local} \tag{4}$$

$$\Leftrightarrow x_{-(\Phi_{local})=\left(\frac{\Phi_{local}\cdot 0.088^{0.228}}{101.5-\Phi_{local}}\right)^{\frac{1}{0.228}}} \tag{5}$$

It represents the described relation for this experimental setup and may likely change for vessels with different S_r and/or hydride-forming alloys.

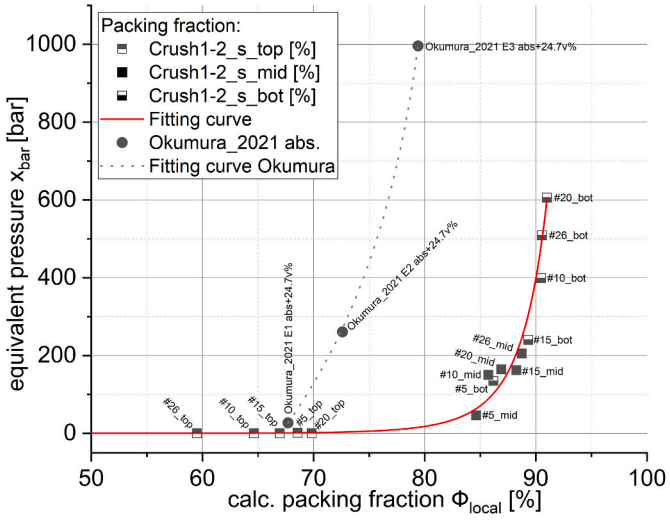

Fig. 8. Relation of calculated packing fraction (based on scans with SRµCT) in an absorbed state to the measured radial stress of the small sample holder. The approximated values, as reported by Okumura et al. [23], have also been incorporated but are indicative only.

When the Φ_{local} value exceeds 70 % in the horizontal plane, an exponential increase in expansion stress is observed. The exponential increase aligns with the findings from Nasako et al. [43] who measured significant differences in stress development when changing the initial packing fraction by only 5 % from 45 to 50 %. To the best of our knowledge, only Okumura et al. [23] have investigated the packing fraction after a defined number of titration cycles and correlated it with radial expansion forces. Their measurement results have been incorporated into the graph in Fig. 8. Since the packing fraction was measured in the desorbed state, a volumetric expansion of 24.7 % (based on the provided specifications) was applied to account for the material's expansion. However, it is important to note that this is a simplified approximation:

Complex effects such as particle rearrangement during absorption and the distinct expansion behavior of AB_5-type alloys are not considered. Plastic deformation of the vessel wall distorts the strain gauge data, likely inflating the measured expansion forces beyond those from elastic deformation alone. Plastic deformation falsely increases their measured expansion forces. As a result, these values are only of limited significance and cannot be directly compared to the purely elastic x_{bar} values defined in this work. Other publications typically report only the initial packing fraction and the stress evolution during titration, without measuring or relating changes in packing fraction throughout the cycling process.

Assuming a storage container homogeneously filled throughout its entire volume with a packing density below this threshold, a similar behavior can be expected along the full height of the container. This observation aligns well with values of Φ' reported in the literature, which identify critical limits for the onset of expansion forces in tank fillings, typically ranging from <40 % to 61 % [43–45]. In the present study, the maximum packing fraction measured via SRµCT was 91 %, corresponding to an expansion stress of 605 bar (*Crush-S1-2_s_bot_#20*). Despite a remaining porosity of 9 %, the expansion stress reached significant levels. Therefore, it indicates potential for further optimization to achieve complete utilization of the available volume V_{cell} or a less confined arrangement of the particles.

Stress evolution varies noticeably across samples. Following Gillia's classification, two curve-types emerge.

(1) Crush_A5T_s_S_20-32_comp. and _maxCompFill show increasing radial stress with cycles before plateauing, which Gillia describes as a saturating evolution ([10], Fig. 9, type (d)).
(2) In contrast, other measurements (Fig. 7) show initially high stress that gradually stabilizes (Gillia [10], Fig. 9, type (f)).

Both evolutions are driven by structural rearrangement and minor pulverization, initial structural reorientation followed by fine fragmentation. The resulting agglomerates efficiently fill pore space during expansion. Given the small particle sizes (20–32 µm, 80–100 µm), pulverization favours cohesive agglomeration near fracture sites over settling or increased bottom-layer stress. Restricted vertical motion due to wall friction may cause early-cycle stress buildup. Further CT analysis could clarify these mechanisms and explain the differing radial stress developments.

4.2. Influence of the particle size distribution

When the fine fraction exceeds 10 % with a particle size of $d_{10} < 5$ µm, agglomeration increases significantly due to the dominance of the van der Waals forces over gravitational forces. This leads to reduced flowability and higher cohesiveness. Such an agglomeration can cause less efficient and more stressful particle rearrangements when tensions arise [46]. Fine powders are referred to as cohesive bulk materials, as particle contacts are inversely proportional to the square of particle size, resulting in stronger adhesive forces than in coarse powders [27]. The

agglomeration can improve the thermal conductivity within the powder bed. However, in the desorbed state Fig. 3 - (6), a gap between the agglomerated powder pillar and container wall impedes thermal conductivity until volume expansion re-establishes contact. At the investigated scale, no measurable effects on thermal conductivity or gas permeation were observed.

Okumura et al. initially used finer particles in a sample holder with a ratio of particle diameter to sample holder diameter of 1:2.5 to 1:25 (for comparison, this work: 1:4 to 1:2) [13]. This particle-to-SH diameter ratio d_p/d_{SH} influences the possible achievable initial packing fraction, Φ', of monomodal powders due to the different possible particle arrangements and, therefore, the developed expansion strain. According to McGeary et al. [47], a high packing fraction Φ' for spherical particles can be achieved when the ratio is 1: (>10). If this ratio significantly deviates, the initial packing density can vary by up to 16 %. Alternatively, the packing fraction can be increased by using polymodal distributions. For example, a polymodal distribution of spheres with a diameter ratio of 1:7:38:316 (four dominating particle sizes) and a related volume composition of 6.1:10.2:23.0:60.07 (%) can increase the packing fraction up to 97.5 % compared to a monomodal PSD with a packing fraction of 62 %. Fine particles can fill the voids between larger particles.

The solid fraction Φ' of the sample holder remains unchanged during the experiments. Φ and Φ' can vary during the hydrogenation-dehydrogenation cycles due to the breathing (see Fig. 3f and h) and reordering of the particles within the bed, leading to a change in V_{hb}.

Bigger particles are more confined in the bottom (and middle) layers, leading to a higher packing fraction. Even though fine powder settles down, larger particles cannot crumble as they do in less densely packed or confined areas. The high confinement and limited particle movement act like an anti-pulverization effect. This phenomenon was observed by Lin et al. [24]: Agglomerates become more compacted and stable with increasing cycles. Due to the increased expansion forces, larger forces arise between the particles, causing the contact areas to deform plastically and decreasing the distances between neighboring particles. This increases the contact surfaces and adhesion forces [27]. In line with SEM measurements, it can be observed that very fine particles tend to agglomerate more readily (Fig. 4a #50).

Based on stress measurements, it can be concluded that the evolution of a continuously increasing and uncontrollable radial expansion stress is caused by a mutative polymodal powder bed, which changes particle shape, size, order, and confinement with each cycle until a steady state is reached. In some cases, the continuation of cycling reaches the limit of the storage vessel before stabilization occurs (*Crush1-2_#20*, Fig. 7). The measured up-and-down equivalent stress pattern described in section 3.2 and Fig. 6a was associated with the continuous reordering of particles within the powder bed during cycling. The stress development changes indicate that no final powder bed state is reached.

4.3. Influence of slenderness ratio

The pressure curves for the sSH (Fig. 6c) show a steady increase with each hydrogenation/dehydrogenation cycle. In contrast, the mSH initially remains unchanged at the same packing fraction Φ'. However, some curves show a drop in radial stress after about eight cycles (Fig. 6a). This difference is linked to the d_p/d_{SH} ratio. SRμCT data reveal that large particles in the sSH tend to get stuck at the bottom, while in the mSH, they can move more freely due to reduced confinement. Lower wall friction weakens stabilization effects by fine powder, resulting in a more uniform PSD within the bed, reduced expansion stress, and improved bed homogeneity.

The slenderness ratio S_r (h_{SH}/d_{SH}) is an important factor influencing the overall system behavior. The mSH has a S_r of 3 (Table 1), slightly below the recommended 3.3 for safety [26], while the sSH reaches 8.75, a factor of 2.6 higher than suggested. As shown in Section 3.2, safety can still be maintained at higher ratios if factors like the PSD are optimized.

Schulze [27] found that higher S_r stabilizes vertical forces, such as natural gravimetric forces, due to increased wall surface area and intensified wall friction, thereby restricting lower-layer expansion and fine particle settlements. SRμCT and PSD data confirm that large particles settle/stay in the lower sSH layers, hindering fine particle migration. This maintains the useful porosity in lower layers (e.g., for selected samples from 3.4).

Higher S_r improves stress reproducibility by limiting powder rearrangement, while larger diameters allow more unrestricted particle movement, increasing variability but better simulating scale-up conditions. According to the Janssen model, slender geometries enhance confinement and stress uniformity, whereas lower ratios reduce reproducibility but facilitate rearrangement.

Literature links a higher S_r to increased swelling stress and more pronounced volume changes [48]. Gillia connects $S_r > 1$ in vertical containers to accelerating stress buildup due to a ratcheting effect from wall friction and recommends $S_r \approx 1$ to balance confinement and swelling accommodation [41]. However, our results show a stabilization of radial stress at a higher $S_r = 8.75$, suggesting that increasing stress is notably influenced by the particle-to-diameter (d_p/d_{SH}) ratio (see 4.2). This result indicates that the stress evolution described in the literature mainly occurs in systems with significant pulverization. For system scaling, it must therefore be evaluated whether the d_p/d_{SH} or the S_r should remain constant or be adapted.

4.4. Mitigation strategies for selected initial particle sizes

The results suggest that adjusting initial powder bed properties can help mitigate detrimental changes in the powder bed evolution without requiring additives or complex treatments.

The PSD measurements after cycling in Fig. 5 show maxima narrowing down the final particle size of the particles in the lower μm range (approx. 2-5 μm), which is similar to the PSD of the cycled samples (see SI Error: Reference source not found).

Powder with a finer initial PSD showed distinct radial stress behavior as compared to coarser particles (*Crush-S1-2*) and results from Qin et al. [11] and Okumura et al. [23]. After filling and compacting the selected powder into the sample holder, an “orientation phase' occurred during the early cycles, characterized by higher radial stresses that then gradually decreased. During the first 10 to 15 hydrogenation-dehydrogenation cycles, the powder particles reorder and utilize the available space and porosity more effectively. Also, slight (though significantly reduced compared to *Crush1-2* samples) pulverization effects contribute to stress reduction during hydrogen absorption (Fig. 5b). This results in a predominant decrease in expansion forces, thereby stabilizing the maximum measured radial stress. The reordering processes within the bed can homogenize the packing fraction and reduce the radial stress, unless friction between particles or to the container wall, confinement, or other factors prevent it.

Larger particles experience more significant size reduction during pulverization (Fig. 5). After the orientation phase, radial stress decreases for 80–100 μm particles, unlike the continued increase seen in 1–2 mm particles. This suggests that greater initial size variation between the initial and final particle sizes results in more unpredictable powder bed behavior. Large particles can also form densely packed regions, including stabilized particles, which generate higher expansion forces (Fig. 8). In contrast, smaller particles create narrower gaps, limiting the downward movement of pulverized material, as also noted by Lin et al. [28].

The bottom section exhibits the most stable radial stress, indicating a steady or final state with sufficiently high porosity. Comparing *Crush_A5T-S_20-32_s_MaxCompFill* and *Crush_A5T-S_80-100_s_MaxCompFill*, finer PSDs lead to a lower packing fraction and lower radial stress in the bottom layer. The consistency proves a reduction of settlement and inhomogeneous densification effects for both PSDs. This leads to less stress and increased bottom-layer strength compared to the typically

measured stress increases, as described in Fig. 7, and prevents plastic deformation ("elephant foot' [11]).

A more confined environment shows beneficial effects for maintaining constant and predictable stress development: Comparing the top sections of *Crush-A5T-S_20-32_comp*, *-MaxCompFill* and *-MaxFill* (Φ" = 51 %, 67 %, and 100 %), the radial force increase from first to last measurement is 450 %, 130 %, and 71 %, respectively, highlighting more substantial changes at lower packing fractions (see percentages in Fig. 7, SI Error: Reference source not found). This is influenced by the available expansion space above the powder bed, allowing for more particle rearrangement. As a result, the powder bed undergoes more changes during hydrogenation/dehydrogenation cycles, reflected in greater changes in radial stress between the first and last cycle.

The absence of larger particles results in less stress development, as shown in Fig. 7 for *Mix Crush-A5T-S_80-100+ C1-2*. The extreme radial stress is unlikely to decrease if more cycles are applied, as the surrounding fine powder particles support these particles. This prevents further pulverization and the increase in porosity, supporting the explanation of the behavior of the *Crush-S1-2* samples.

Based on the obtained outcomes and performed analysis, it is possible to propose three main strategies to reduce the stress caused by swelling of metal hydrides effectively.

(1) Utilizing a fine powder with particle sizes close to the final particle size;
(2) Utilizing a pre-compressed powder;
(3) Utilizing the whole cell volume with sufficient porosity

As shown in Fig. 9, the strategies influence the development of the powder bed and contribute to controlling radial expansion stress.

5. Summary, conclusions, and outlook

In this work, the development of radial expansion forces in vertically placed storage containers filled with AB_2 hydride-forming alloy powder (commercially available Hydralloy C5) was investigated by applying advanced characterization techniques. The main outcomes and prospects can be summarized as follows.

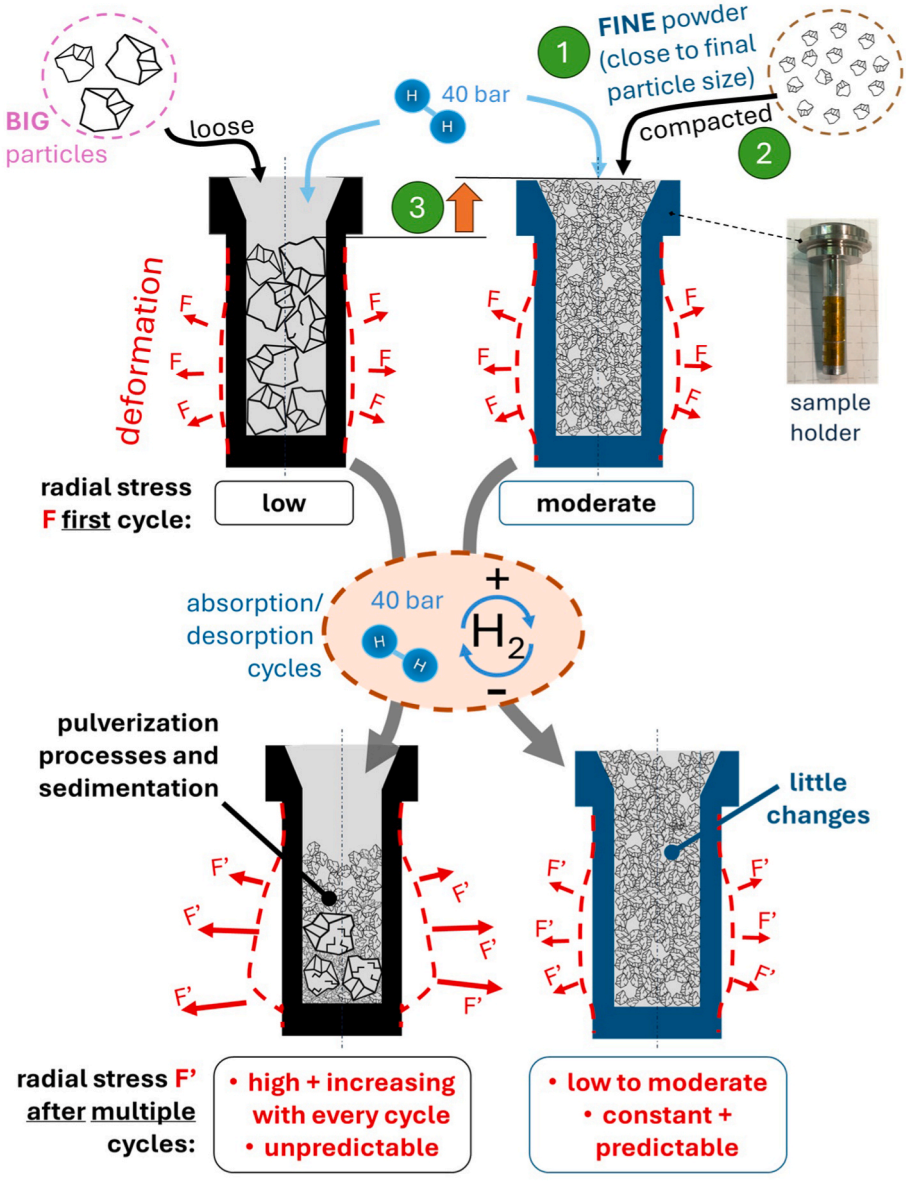

Fig. 9. Schematic illustration of radial stress mitigation strategies in hydrogen storage vessels.

- Characterizations (SEM, PSD, volumetric analysis, and SRμCT) suggest that high, unpredictable radial expansion stress originates from a dynamic powder bed that changes particle shape, size, and packing with each hydrogenation/dehydrogenation cycle. During absorption/desorption, particles fracture into 2-5 μm, benefiting agglomeration. These fine particles sediment towards the bottom of the SH and settle around larger ones (1–2 mm), hindering their pulverization and increasing the local packing fraction to up to 91% in the absorbed state. This leads to increased expansion stress in lower layers. During desorption, an annular gap forms, allowing continued sedimentation of fine particles.
- An empirical equation describes the equivalent internal pressure by particle expansion depending on the local packing fraction from the SRμCT data, showing an exponential stress growth at the packing fraction Φ_{local} higher than 70 % in the hydride state. Previous studies have focused on characterizing elastic deformation [23]. In this work, to the best of our knowledge, it is the first time that an equation linking packing density and elastic tank expansion has been developed.
- Establishing a stable, pre-compressed powder bed using initially fine particles, ranging from 20 to 32 μm, is beneficial for maintaining a stable and controllable radial stress development over multiple cycles. After 20 cycles, the stress was notably reduced by 45 %, compared to the initial use of 1-2 mm (*Crush-S1-2_#20*) with activated and sieved MH powder (*Crush1-2_S20-32_A5T_maxFill*). Although the MH mass increased by 87%, the expansion-induced stress stabilized or even decreased with progressing cycles for the latter. Both measurements reached the maximum hydrogen capacity. The selected particle size distribution demonstrates how packing density can be increased without the need for additives or system modifications, while maintaining lower and more stable expansion forces.
- During the first hydrogenation cycles of manually compacted powder beds with a small initial particle size, an 'orientation phase' was observed: Higher radial stress occurred predominantly during the first approximately 4 hydrogenation-dehydrogenation cycles. Afterwards, particles are reordered into a more relaxed state, reducing stress during hydrogen absorption.

This study introduces a novel method to enhance the performance of metal hydride (MH) powder beds without compromising hydrogen capacity, causing thermodynamic shifts, or introducing kinetic limitations. It also lays the groundwork for further research on optimizing MH storage systems for both stationary and mobile applications, paving the way for a clean, emission-free future.

CRediT authorship contribution statement

G. Stahlkopf: Conceptualization, Data curation, Formal analysis, Investigation, Methodology, Validation, Visualization, Writing – original draft, Writing – review & editing. **M. Passing:** Conceptualization, Formal analysis, Methodology, Supervision, Writing – review & editing. **J.A. Puszkiel:** Conceptualization, Methodology, Supervision, Writing – review & editing. **J. Moosmann:** Data curation, Formal analysis, Writing – review & editing. **F. Beckmann:** Data curation, Formal analysis. **J. Warfsmann:** Data curation, Formal analysis, Writing – review & editing. **F. Karimi:** Data curation, Formal analysis, Writing – review & editing. **V. Kulvait:** Data curation, Formal analysis. **T. Klassen:** Conceptualization, Funding acquisition, Project administration, Resources, Supervision, Writing – review & editing. **J. Jepsen:** Conceptualization, Funding acquisition, Project administration, Resources, Supervision, Writing – review & editing.

Declaration of competing interest

The authors declare that they have no known competing financial interests or personal relationships that could have appeared to influence the work reported in this paper.

Acknowledgement

The authors gratefully acknowledge the funding by Bundesministerium für Wirtschaft und Klimaschutz in the frame of the “HyReflexS “project (Funding code: 03El3020A and 03EI3020C). This research work is also in the frame of the project Digi-HyPro, funded by dtec.bw – Digitalization and Technology Research Center of the Bundeswehr, which the authors gratefully acknowledge. dtec.bw is financed by the European Union – NextGenerationEU. We acknowledge the Deutsches Elektronen-Synchrotron (DESY, Hamburg, Germany), a member of the Helmholtz Association HGF, for the provision of experimental facilities. Parts of this research were carried out at PETRA III at the high-energy materials science (HEMS) beamline P07, operated by Helmholtz-Zentrum Hereon. Beamtime was allocated for proposal I-20230862.We would like to thank Ursula Tietze for her assistance during the experiments. We would like to thank Dr. Florian Wieland from the Helmholtz-Zentrum Hereon, Institute for Metallic Biomaterials, for his support in conducting feasibility studies using a conventional CT. This research was partly supported by the Maxwell computational resources operated at DESY.

Appendix A. Supplementary data

Supplementary data to this article can be found online at https://doi.org/10.1016/j.ijhydene.2026.153776.

List of abbreviations and symbols

CT	Computed tomography
DESY	Deutsches Elektronen-Synchrotron
MH	Metal hydrides
PSD	Particle size distribution
SEM	Scanning electron microscopy
SH	Sample holder
mSH	Medium SH
sSH	Small SH
SI	Supportive information
US	Ultrasonic treatment
Φ	Solid volume related to powder bed volume
Φ'	Solid volume related to cell volume

(*continued on next page*)

(*continued*)

Φ"	Powder bed volume related to cell volume
Φ_{local}	Local packing fraction
d_{10}	Percentile size, 10 % of the particles are smaller than d_{10}
d_p	particle diameter
d_{SH}	SH inner diameter
S_r	Slenderness ratio
V_s	Volume of solid sample material
V_{cell}	Volume of sample holder
V_{hb}	Volume of powder bed incl. Porosity
x_{bar}	Equivalent inner pressure

References

[1] Dincer I, Aydin MI. New paradigms in sustainable energy systems with hydrogen. Energy Convers Manag 2023;283. https://doi.org/10.1016/j.enconman.2023.116950.

[2] Drawer C, Lange J, Kaltschmitt M. Metal hydrides for hydrogen storage – identification and evaluation of stationary and transportation applications. J Energy Storage 2024;77. https://doi.org/10.1016/j.est.2023.109988.

[3] Bundesministerium für Wirtschaft und Klimaschutz. Weißbuch Wasserstoffspeicher bmwk.de; 2025.

[4] Fleiter T, Fragoso J, Lux B, Alibaş Ş, Al-Dabbas K, Manz P, et al. Hydrogen infrastructure in the future CO2-Neutral european energy system—how does the demand for hydrogen affect the need for infrastructure? Energy Technol 2025;13:2300981. https://doi.org/10.1002/ENTE.202300981.

[5] Dematteis EM, Berti N, Cuevas F, Latroche M, Baricco M. Substitutional effects in TiFe for hydrogen storage: a comprehensive review. Mater Adv 2021;2:2524–60.

[6] Bellosta von Colbe J. 2018_VColbe_Application of hydrides in hydrogen storage and compression Achievements, outlook and perspectives. Int J Hydrogen Energy 2019;44(15):7780–808. https://doi.org/10.1016/j.ijhydene.2019.01.104.

[7] Rusman NAA, Dahari M. A review on the current progress of metal hydrides material for solid-state hydrogen storage applications. Int J Hydrogen Energy 2016;41:12108–26. https://doi.org/10.1016/j.ijhydene.2016.05.244.

[8] Puszkiel JA, Andrade-Gamboa JJ, Gennari FC. Recent progress in mg–co–h and mg–fe–h systems for hydrogen energy storage applications. Emerging Materials for Energy Conversion and Storage 2018:393–428. https://doi.org/10.1016/B978-0-12-813794-9.00012-0.

[9] Scarpati G, Frasci E, Di Ilio G, Jannelli E. A comprehensive review on metal hydrides-based hydrogen storage systems for mobile applications. J Energy Storage 2024;102. https://doi.org/10.1016/j.est.2024.113934.

[10] Gillia O. Hydride breathing and its consequence on stresses applied to containers: a review. Int J Hydrogen Energy 2021;46:35594–640. https://doi.org/10.1016/j.ijhydene.2021.07.082.

[11] Qin F, Chen J, Chen Z. The hydriding-dehydriding characteristics of La0.6Y0.4Ni4.8Mn0.2 and their influences in the surface strain on small-scale, thin-wall and vertical containers. Mater Des 2008;29:1926–33. https://doi.org/10.1016/j.matdes.2008.04.024.

[12] Yang FS, Wang GX, Zhang ZX, Meng XY, Rudolph V. Design of the metal hydride reactors – a review on the key technical issues. Int J Hydrogen Energy 2010;35:3832–40. https://doi.org/10.1016/J.IJHYDENE.2010.01.053.

[13] Okumura M, Segawa Y, Endo N. Investigation of the internal pressure exerted by a $LaNi_5$ bed on a vertical cylindrical vessel and its packing fraction distribution during Cyclic Hydrogen Ab/Desorption. ACS Appl Energy Mater 2025. https://doi.org/10.1021/acsaem.4c02916.

[14] Koochacsaraiy RK, Goudarzi AM, Morshedsolouk F. Mechanical behavior of metal hydrides and hydrogen storage containers: a review. Hydrogen. Fuel Cell and Energy Storage 2023;10:257–78. https://doi.org/10.22104/HFE.2024.6623.1277.

[15] Warfsmann J, Puszkiel JA, Passing M, Krause PS, Wienken E, Taube K, et al. Applying wash coating techniques for swelling-induced stress reduction and thermal improvement in metal hydrides. n.d.

[16] Heubner F, Pohlmann C, Mauermann S, Kieback B, Röntzsch L. Mechanical stresses originating from metal hydride composites during cyclic hydrogenation. Int J Hydrogen Energy 2015;40:10123–30. https://doi.org/10.1016/j.ijhydene.2015.06.053.

[17] Au MG. Some engineering methods for eliminating deformation and expansion damage of hydride storage containers. J Less Common Met 1961;172:1168–74.

[18] Puszkiel JA, Neves AM, Warfsmann J, Krause PS, Kaufmann TFJ, Hoberg AR, et al. On the hydrogen storage properties and life cycle evaluation of a room temperature hydride for scale-up applications: the case of an AB2-alloy. Int J Hydrogen Energy 2025;118:482–99. https://doi.org/10.1016/J.IJHYDENE.2025.03.161.

[19] Cuscueta DJ, Silin N, Melnichuk M. Stress reduction in a hydride container by the addition of a glidant agent. Int J Hydrogen Energy 2020;45:27452–6. https://doi.org/10.1016/J.IJHYDENE.2020.07.020.

[20] Meyer K, Zimmermann I. Effect of glidants in binary powder mixtures. Powder Technol 2004;139:40–54. https://doi.org/10.1016/J.POWTEC.2003.09.007.

[21] Wang QD, Wu J, Chen CP, Li ZP. An investigation of the mechanical behaviour of hydrogen storage metal beds on hydriding and dehydriding and several methods of preventing the damage of hydride containers caused by the expansion of hydrogen storage metals. Journal of the Less Common Metals 1987;131:399–407. https://doi.org/10.1016/0022-5088(87)90539-X.

[22] Zheng X, Kong H, Chu D, Hu F, Wang Y, Yan Y, et al. Stress reduction of a V-Based BCC metal hydride bed using silicone oil as a glidant. INORGA 2022;10:167. https://doi.org/10.3390/INORGANICS10100167. 2022;10:167.

[23] Okumura M, Terui K, Ikado A, Saito Y, Shoji M, Matsushita Y, et al. Investigation of wall stress development and packing ratio distribution in the metal hydride reactor. Int J Hydrogen Energy 2012;37:6686–93. https://doi.org/10.1016/j.ijhydene.2012.01.097.

[24] Okumura M, Ikado A, Saito Y, Aoki H, Miura T, Kawakami Y. Pulverization mechanism of hydrogen storage alloys on microscale packing structure. Int J Hydrogen Energy 2012;37:10715–23. https://doi.org/10.1016/j.ijhydene.2012.04.061.

[25] Galvis Escobar AR, Chaise A, Iosub V, Salque B, Fernandez JF, Gillia O. Stress effect on the swelling/shrinking behavior of an AB2 alloy during hydrogenation cycles. Int J Hydrogen Energy 2017;42:22422–31. https://doi.org/10.1016/j.ijhydene.2017.03.145.

[26] Tran DP, La MP, Lototskyy MV. Stress analysis of cyclic sorption-desorption in metal hydride vessels. J Energy Storage 2024;98. https://doi.org/10.1016/j.est.2024.112868.

[27] Schulze Dietmar. Pulver und Schüttgüter. Fließeigenschaften und Handhabung. 2019. p. 9–98. https://doi.org/10.1007/978-3-662-58776-8.

[28] Lin CK, Huang SM, Jhang YH. Effects of cyclic hydriding–dehydriding reactions of Mg2Ni alloy on the expansion deformation of a metal hydride storage vessel. J Alloys Compd 2011;509:7162–7. https://doi.org/10.1016/J.JALLCOM.2011.04.038.

[29] Haas I, Schott E. The effect OF mechanical stress ON the ABSORPTION OF hydrogen BY metal hydrides, vol. 16; 1991.

[30] Borzenko VI, Romanov IA, Dunikov DO, Kazakov AN. Hydrogen sorption properties of metal hydride beds: effect of internal stresses caused by reactor geometry. Int J Hydrogen Energy 2019;44:6086–92. https://doi.org/10.1016/j.ijhydene.2019.01.052.

[31] Ao BY, Chen SX, Jiang GQ. A study on wall stresses induced by LaNi5 alloy hydrogen absorption–desorption cycles. J Alloys Compd 2005;390:122–6. https://doi.org/10.1016/J.JALLCOM.2004.05.092.

[32] Biasetti A, Marín J, Meyer G, Borzone EM, Aversente N, Baruj A. Decrepitation process of a hydride forming material observed by neutron radiography. J Phys, Conf Ser 2023;2605. https://doi.org/10.1088/1742-6596/2605/1/012033.

[33] Matsushita M, Tajima I, Abe M, Tokuyama H. Experimental study of porosity and effective thermal conductivity in packed bed of nano-structured FeTi for usage in hydrogen storage tanks. Int J Hydrogen Energy 2019;44:23239–48. https://doi.org/10.1016/j.ijhydene.2019.07.037.

[34] Puszkiel JA, Neves AM, Warfsmann J, Krause PS, Kaufmann TFJ, Hoberg AR, et al. On the hydrogen storage properties and life cycle evaluation of a room temperature hydride for scale-up applications: the case of an AB 2-alloy. Int J Hydrogen Energy 2025;118:482–99. https://doi.org/10.1016/j.ijhydene.2025.03.161.

[35] Brüel Hottinger, GmbH Kjaer. M series - strain gages for experimental stress analysis; Data sheet -B5399. Im Tiefen See 45, 64293 Darmstadt, Germany 2024.

[36] Brüel Hottinger, GmbH Kjaer. Y series; Strain gages. Data sheet; 2024. B04709. Im Tiefen See 45, 64293 Darmstadt, Germany.

[37] Walter C, Jepsen J, Maschinenbau F. Entwicklung einer Messzelle zur Untersuchung der Partikelexpansion von Metallhy-driden. n.d.

[38] Schell N, King A, Beckmann F, Fischer T, Müller M, Schreyer A. The high energy materials science beamline (HEMS) at PETRA III. Mater Sci Forum 2014;772:57–61. https://doi.org/10.4028/WWW.SCIENTIFIC.NET/MSF.772.57.

[39] Lautner S, Lenz C, Hammel JU, Moosmann J, Kühn M, Caselle M, et al. Using SRuCT to define water transport capacity in Picea abies 2017;10391:180–6. https://doi.org/10.1117/12.2287221.

[40] Kulvait V, Moosmann J, Rose G. Cutting voxel projector a new approach to construct 3D cone beam CT operator. J Comput Sci 2025;87:102573. https://doi.org/10.1016/J.JOCS.2025.102573.

[41] Li Y, Chang J, Zhang X, Wu H, Huang Y, Zhang Y, et al. Study on the stress accumulation characteristics of a rotating metal hydride reactor. Int J Hydrogen Energy 2025;97:959–69. https://doi.org/10.1016/j.ijhydene.2024.11.463.

[42] Blinov DV, Dunikov DO, Kazakov AN, Romanov IA. Influence of geometrical non-uniformities of LaNi5 metal hydride bed on its structure and heat and mass transfer at hydrogen absorption. In: J Phys conf ser, vol. 891. Institute of Physics Publishing; 2017. https://doi.org/10.1088/1742-6596/891/1/012119.

[43] Nasako K, Ito Y, Hiro N, Osumi M. Stress on a reaction vessel by the swelling of a hydrogen absorbing alloy, vol. 264; 1998.
[44] Yang FS, Wang GX, Zhang ZX, Meng XY, Rudolph V. Design of the metal hydride reactors - a review on the key technical issues. Int J Hydrogen Energy 2010;35:3832–40. https://doi.org/10.1016/j.ijhydene.2010.01.053.
[45] Saito T, Suwa K, Kawamura T. Influence of expansion of metal hydride during hydriding-dehydriding cycles, vol. 253; 1997.
[46] Spierings AB, Levy G. Comparison of density of stainless steel 316L parts produced with selective laser melting using different powder grades. n.d.
[47] McGEARY RK. Mechanical packing of spherical particles. J Am Ceram Soc 1961;44:513–22. https://doi.org/10.1111/j.1151-2916.1961.tb13716.x.
[48] Wu Z, Guo T, Li X, Liu H, Wang B, Yao J, et al. An overview of swelling stress formation and control of metal hydride for high-safety and high-density hydrogen storage applications. Appl Energy 2025;402:126909. https://doi.org/10.1016/J.APENERGY.2025.126909.